Title
Autonomous wearable sweat rate monitoring based on digitized microbubble detection.

Journal
Lab on a Chip, 22(22)

Authors
Lin, Haisong
Yu, Wenzhuo
Suarez, Jorge
et al.

Publication Date
2022-11-08

DOI
10.1039/d2lc00670g

Peer reviewed

HHS Public Access

Author manuscript

Lab Chip. Author manuscript; available in PMC 2023 November 08.

Published in final edited form as:

Lab Chip. ; 22(22): 4267–4275. doi:10.1039/d2lc00670g.

Autonomous wearable sweat rate monitoring based on digitized microbubble detection

Haisong Lin[‡,*,a,b], **Wenzhuo Yu**[‡,a], **Jorge Emiliano De Dios Suarez**[a], **Harish Athavan**[a], **Yibo Wang**[a], **Chris Yeung**[c], **Shuyu Lin**[a], **Sriram Sankararaman**[d], **Carlos Milla**[e], **Sam Emaminejad**[*,a]

[a]Department of Electrical and Computer Engineering, UCLA

[b]Department of Mechanical Engineering, University of Hong Kong

[c]Department of Material Science and Engineering, UCLA

[d]Department of Computer Science, UCLA

[e]Stanford School of Medicine, Stanford University

Abstract

Advancements in wearable bioanalytical microsystems have enabled diurnal and (semi)continuous monitoring of physiologically-relevant indices that are accessible through probing sweat. To deliver an undistorted and physiologically-meaningful interpretation of these readings, tracking the sweat secretion rate is essential, because it allows for calibrating the biomarker readings against variations in sweat secretion and inferring the body's hydration/electrolyte homeostasis status. To realize an autonomous wearable solution with intrinsically high signal-to-noise ratio sweat rate sensing capabilities, here, we devise a digitized microbubble detection mechanism—delivered by a hybrid microfluidic/electronic system with a compact footprint. This mechanism is based on the intermittent generation of microliter-scale bubbles *via* electrolysis and the instantaneous measurement of their time-of-flight (and thus, velocity) *via* impedimetric sensing. In this way, we overcome the limitations of previously proposed sweat rate sensing modalities that are inherently susceptible to non-targeted secretion characteristics (pH, conductivity, and temperature), constrained by volume, or lack system integration for autonomous on-body operation. By deploying our solution in human subject trials, we validate the utility of our solution for seamless monitoring of exercise- and iontophoretically-induced sweat secretion profiles.

Graphical Abstract

A digitized microbubble detection mechanism delivered by a hybrid microfluidic/electronic system is devised for autonomous wearable high signal-to-noise ratio sweat rate monitoring.

[*]Corresponding author: emaminejad@ucla.edu; linhs@hku.hk.

[‡]These authors contributed equally: Haisong Lin, Wenzhuo Yu

Author contributions

H.L., and S.E. conceived the study idea and contributed to the design of experiments. H.L., and W.Y. led the experiments with assistance from J.E.D.D.S., H.A., Y.W., S.L.. H.L., W.Y., J.E.D.D.S., H.A., Y.W., S.L., S.S., C.M., and S.E. contributed to analytical tools and data analysis. H.L., and S.E. drafted the manuscript, and all the authors provided feedback.

Conflicts of interest

The authors declare no competing interests.

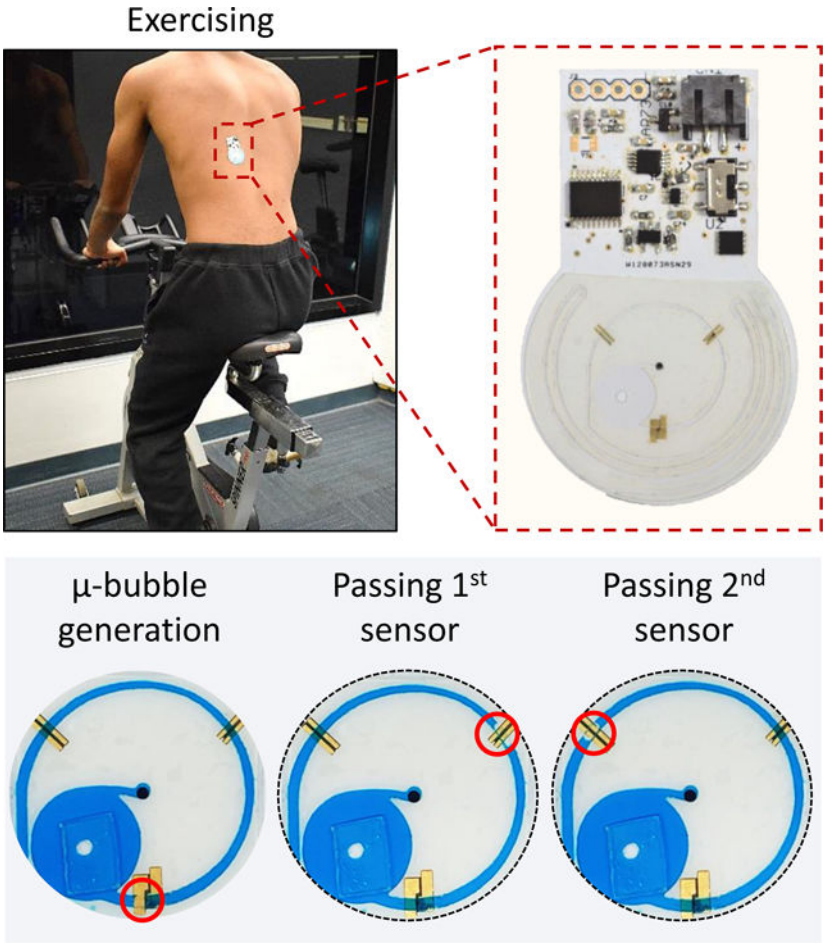

1. Introduction

Advancements in wearable bioanalytical microsystems have paved the path for a new generation of personalized health and fitness monitoring electronics that provide insight into the body's dynamic physiological status (such as metabolism and hydration) by continuously and noninvasively monitoring sweat composition and secretion characteristics[1–6]. Recently developed wearable sweat sensing systems successfully demonstrated the measurement of a wide variety of biomarkers such as electrolytes[7–9] (*e.g.* sodium, potassium, calcium, and chloride), metabolites[10, 11] (*e.g.* glucose, lactate, and uric acid), and xenobiotics[12–15] (*e.g.* caffeine, ethanol, and pharmaceuticals). However, due to the complex nature of sweat secretion and reabsorption, the concentrations of biomarkers quantified in epidermally-retrieved sweat may be influenced by irregularities in sweat secretion rates, thus confounding interpretations based on raw sweat biomarker measurements[16–18]. Furthermore, we have recently illustrated that variation in sweat rate can significantly affect the reaction-based sensors' responses, due to the sweat secretion's role in facilitating the advective analyte transport/delivery to the sensing interface[19]. Therefore, to reliably deliver physiologically-meaningful and undistorted measures of sweat biomarkers, capturing the sweat secretion rate profile is necessary for calibration purposes. Moreover,

the sweat rate information is useful—as a standalone parameter—for the assessment of the body's hydration/electrolyte homeostasis status and to inform personalized preventative or cautionary measures (such as immediate or periodic supplemental intake/rehydration)[20–22].

Previously reported sweat rate sensors that are based on the measurement of impedance/temperature changes induced by liquid flow[23, 24] are fundamentally sensitive to natural variations in the physical and chemical properties of sweat (temperature, pH, ionic strength, *etc.*). These natural variations will either cause inaccurate sensing results or require a complex calibration system to rectify the sweat rate measurement. Alternatively demonstrated sweat rate sensing solutions that are based on electrical/optical monitoring the physical migration of sweat along a predefined microfluidic channel is inherently constrained by the total secreted sweat volume[24–27], necessitating repeated sensor unit replacement. Recently, a digital microfluidic-based sweat rate sensing interface was proposed that addresses such shortcomings by passively converting the continuous sweat stream into equally-sized droplets, which are subsequently counted with the aid of a mesh electrode, effectively rendering high signal-to-noise ratio (SNR) measurements[28]. However, further development is necessary to integrate the microfluidics and electronics components for wireless signal acquisition and practical applications.

Here, we devised a digitized microbubble detection mechanism—delivered by a wearable hybrid microfluidic/electronic system with autonomous functionality—that overcomes the limitations of previously investigated sweat rate sensors. This mechanism is based on intermittent generation of microliter-scale bubbles ("μ-bubbles") within a microfluidic channel by utilizing a programmable electrolysis electrode pair, and subsequently, inferring the velocity of individual μ-bubbles by measuring their time-of-flight as they pass through two pairs of impedance sensing electrodes. Due to the orders of magnitude difference in the conductivity of air *vs.* sweat, the passage of each μ-bubble above each of the electrode pairs translates into a spike in the impedimetric baseline measurement that is insensitive to interference and dynamic changes to the physical/chemical properties of sweat as well as the surrounding environment. In this manner, we can achieve high SNR measurements. Furthermore, since the system tracks the iteratively-generated μ-bubble flow instead of the total liquid volume change, the sweat rate sensing mechanism is not volume-constrained. To render autonomous functionality, we integrated the digitized μ-bubble detection interface into a miniaturized custom-developed printed circuit board (PCB), equipped with wireless and programmable excitation and sensing circuitries. To validate the utility of our system for on-body applications, we utilized it to monitor the iontophoretically- and exercise-induced sweat secretion profiles in human subject trials.

2. Results and discussion

2.1 Overview of system design and operational principle

Our sweat rate sensing system is developed by following a hybrid microfluidic/electronic module design and adhesion-based vertical integration scheme. As shown in Fig. 1a and Supplementary Fig. 1a, from top to bottom, our system consists of: 1) a Polyethylene terephthalate (PET)-based microfluidic module with a spiral serpentine channel and surfactant reservoir fabricated from laser-cut double-sided tape; 2) a PCB module featuring

electrolysis and impedance sensing electrode pairs for repeatable μ-bubble generation and tracking, as well as miniaturized wireless excitation/sensing circuitries to render autonomous functionality; 3) a skin-adhesive film for sweat collection. We specifically incorporated overlaying orifices within these three components to fluidically connect the top microfluidic module and sweat collection module (effectively, forming a fluidic vertical interconnect access, or VIA).

This fully-integrated hybrid system is realized within a compact footprint (5 cm^2), making it easily attachable—as a self-sustaining unit—to most body parts (*e.g.*, arms and back) *via* robust adhesion[29]. Once the device is applied on the skin and interfaced with actively secreting sweat glands, the gland-generated fluidic pressure naturally forces the accumulated sweat within the collection chamber to flow into the top microfluidic channel through the dedicated VIA. At the inlet of the channel, a 7-μL surfactant reservoir is incorporated to promote the progression of the subsequently-generated μ-bubble in the channel (Fig. 1b). A complete cycle of the sweat rate sensing mechanism is demonstrated in Fig. 1c and Supplementary Fig. 1b. A μ-bubble is generated *via* electrolysis by applying a potential difference of 5 V across the pair of electrolysis electrodes for a few seconds (*e.g.*, 5 s). After switching off the excitation voltage, the μ-bubble follows the fluid flow within the channel towards the sensing electrodes. When the μ-bubble reaches each of the two neighboring sensing electrode pairs, the original electrode/liquid interface is transformed into an electrode/gas interface. This change manifests as a large increase in the continuously measured impedance from Z_{low} to Z_{high} due to the orders of magnitude lower electrical conductivity of air as compared to that of the biofluid. By calculating the time between the two impedance peaks (corresponding to the passage of the μ-bubble across each of the neighboring sensing electrode pairs), we can calculate the speed of the μ-bubble and infer the flow rate of the fluid inside the channel. Since our flow rate sensing methodology is based on tracking the movement of intermittently generated μ-bubbles instead of measuring the time derivative of the total liquid volume change (the basis of operations for the majority of the conventional wearable sweat sensors), the system's overall functions can be maintained even when the fluidic channel is completely filled. This feature makes our solution suitable for prolonged sweat rate monitoring.

2.2 Design and characterization of the microfluidic system

Electronic programmability of the electrolysis interface inherently allows us to precisely control the μ-bubble size. To illustrate this point, as shown in Fig. 2a, by varying the actuation time from 1 to 8 seconds, we generated different volumes of μ-bubbles. The observed high-confidence linear relationship between the actuation time and the generated μ-bubble's volume ($R^2 = 0.99$) indicates our high degree of controllability and precision in tuning the μ-bubble volumes—a capability which could be useful for adapting our μ-bubble-based solution for different electrode/channel geometries.

To promote the unimpeded progression of the generated μ-bubble along the channel, a 7 μL surfactant reservoir is incorporated at the inlet of the microfluidic channel, which effectively mixes the surfactant with the collected sweat sample (Fig. 1). This mixture lowers the surface tension at the gas/fluid interface of the μ-bubble, thus increasing the ratio of the

viscous drag forces over the surface tension forces, and ultimately smoothing the μ-bubble flow[30]. The utility of the surfactant is demonstrated in Fig. 2b, where the generated μ-bubble moves freely and in tandem with the fluid flow within the channel when the fluid sample is treated *in-situ* upon entry (*via* an embedded surfactant reservoir upstream), while with no surfactant treatment, the generated μ-bubble remains stationary within the fluid flow.

To detect the μ-bubble's velocity inside the microchannel, two pairs of impedance sensing electrodes were incorporated downstream of the electrolysis electrodes. Our inherently high SNR measurements gave us the flexibility to simplify the readout circuitry. Instead of allocating two dedicated impedance monitoring channels (one for each of the impedance sensing electrode pairs, namely, R_1 and R_2), we utilized a single channel to monitor the changes of the measured impedance by leveraging a parallel configuration of the two electrode pairs (*i.e.*, $R_1 \parallel R_2$). In the latter implementation, the passage of the μ-bubble across either of the electrode pairs leads to a spike in the single-channel impedance measurement. It is worth noting that while this parallel implementation lowers the amplitude of the impedance spike in comparison to the former case, it does not affect the accuracy of the end-point assessment (*i.e.*, the processed signal practically remains unaffected).

Figure 2c illustrates the equivalent circuit model of the electrodes/fluid interface in relation to the instantaneous position (P_i) of the μ-bubble (for the devised parallel configuration). When the μ-bubble is not passing over the sensing electrode pairs (*e.g.*, entry point P_1, in between the two electrode pairs P_3, and exit point P_5), the impedance measurement corresponds to the baseline measurement of $R_0 = (R_1 \parallel R_2)$. When the μ-bubble passes over the first or second sensing electrode pairs (P_2 and P_4) the measured impedance increases to $(R_1+\Delta R) \parallel R_2$ or $R_1 \parallel (R_2+\Delta R)$. Given that the conductivity of the air is orders of magnitude lower than sweat, the incremental impedance components ΔR is much larger than the baseline measurements of R_1 or R_2, leading to measured spike amplitudes $\approx R_1$ or R_2 ($2R_0$). Our continuous single-channel impedance recordings validate this pattern (Fig. 2d).

2.3 *Ex situ* sweat rate sensing characterization

To evaluate the flow rate sensing capabilities of the devised methodology, we performed *ex situ* characterization studies. As shown in Fig. 3a, to test our measurement capability at a range of controlled flow rates, we connected a programmable syringe pump to our microfluidic/electronic device (with electrodes patterned and actuation circuits on a PCB substrate), and utilized an external potentiostat to continuously record the impedance across the parallel configuration of the two sensing electrode pairs. The impedance recordings were post-processed, following binary thresholding and pulse-width narrowing steps, to extract peaks corresponding to the passage of the generated μ-bubbles (Fig. 3b). Given our envisioned application, the pump's input flow rate was programmed to different levels within the range of 0.6 μL/min to 10 μL/min (corresponding to the human physiological sweat rate range). At each flow rate input level, multiple sensor readings were assessed to evaluate our devised sensing mechanism's accuracy, repeatability, and reliability. As shown in Figure 3c, each sequential pair of spikes reflects the passage of the μ-bubble over the first or the second electrode pair. The measured flow rate was then calculated by using the recorded time intervals between the impedance spike pairs and the volume

of the microfluidic channel. As a result, we observe in the Fig. 3c that the time interval between the spike pairs decreases as the input flow rate increases from 0.6 to 10 μL/min. To assess the accuracy of our measured flow rate in comparison to the real input flow rate, a calibration curve was plotted in Fig. 3d. The calibration results yielded a highly linear relationship between the measured flow rates and the input flow rates ($R^2 = 0.997$).

Additionally, toward adapting our flow rate sensing mechanism for on-body sweat rate monitoring, we performed dedicated characterization studies to assess the potential influence of naturally-varying sweat conditions on the sensor readings. We specifically characterized our flow rate sensing mechanism's robustness and accuracy against variations in the input fluid's pH, ionic strength, and the surrounding temperature (major shortcomings of the previously reported sweat rate sensors). As illustrated in Fig. 3e–g, the results collectively illustrate our sensing mechanism's high degree of robustness: minimal sensor readout variations were observed for the same flow rate input (< 1.8%), despite changes to the introduced fluid's pH (= 6, 7, and 8), ionic strength (= 1 mM, 0.33 mM, 0.1 mM, Na^+ in phosphate buffered saline, PBS), and surrounding temperature (from 30°C to 44 °C).

2.4 Wearable sweat rate monitor implementation

By integrating the sweat collector, the control and sensing circuitry, and the microfluidic channel, a microfluidic/electronic wearable device is created for on-body sweat rate monitoring. Before the application of the device on body, we validated the preservation of surfactant within our device over time and under shaking conditions (Supplementary Fig. 2&3). Figure 4a,b illustrate the system-level implementation of the miniaturized wearable circuitry. At its core, the circuit board utilizes a microcontroller unit (MCU) to control μ-bubble actuation and enable impedance measurement operations, which interfaces with an onboard Bluetooth transceiver to wirelessly communicate with a smartphone. The μ-bubble generation circuit consists of a voltage regulator for consistent excitation power delivery and an MCU-controlled programmable switch for generating μ-bubbles at user-specified time points. The impedance between the sensing electrode pairs is measured by utilizing an inverting amplifier and programmable function generator chip, then an analog-to-digital (ADC, in the MCU) channel is used to convert the analog readout signal (from the amplifier) to the digital domain. The mobile application sends the operation commands to the MCU and retrieves the measured sweat rate data in real-time.

To validate the suitability and reliability of our integrated device for on-body sweat rate monitoring, we applied our device to track iontophoretically- and exercise-induced sweat secretion profiles of human subjects. Figure 4c demonstrates the mechanism and set-up of the iontophoresis experiment. Before the sweat rate sensor was applied on-body, an iontophoresis instrument was equipped to the forearm of the subject to deliver the sweat stimulation agonist, pilocarpine, to the subject's sweat glands. After 5 minutes of stimulation, the iontophoresis instrument was removed, and the sweat rate sensor was placed on the subject's forearm (at the anodic iontophoresis region) to initiate the sweat rate monitoring process (Fig. 4d). Figure 4e shows the monitored sweat rate profile, where a decreasing sweat rate is observed over the course of 15 minutes. This decreasing trend is attributed to the removal of the iontophoresis stimulation 10 minutes prior to the start of the

measurement, which caused the sweat glands to become less active over time. Furthermore, the sweat rate sensing system was also applied to the back of the human subjects to validate its utility during exercising activities (Fig. 4f). In Fig. 4g,h, the measured sweat rates of two subjects undergoing two different exercising schedules are shown. Specifically, as seen from Fig. 4g, when the exercising intensity increased from 900 s to 1100 s, the sweat rate increased from 3 μL/min to 8 μL/min. In Fig. 4h, when the intensity decreased from 900 s to 1300 s and increased after 1300 s, the sweat rate decreased from 5 μL/min to 2 μL/min and increased from 2 μL/min to 4 μL/min, respectively. The results demonstrate that when the exercising intensities change, the sweat rate is affected proportionately.

3. Conclusion

We report a digitized microbubble detection mechanism for wearable sweat rate sensing —delivered by a hybrid microfluidic/electronic system. This mechanism is based on the intermittent generation of microliter-scale bubbles *via* electrolysis and the instantaneous measurement of their time-of-flight (and thus, velocity) *via* impedimetric sensing. *Ex situ* experiments reveal high-accuracy sweat rate measurements in comparison to pre-programmed input flow rates. In this manner, we overcome the limitations of previously proposed sweat rate sensing modalities, which are based on the measurement of impedance/temperature changes induced by liquid flow that are fundamentally sensitive to natural variations in the physical and chemical properties of sweat (temperature, pH, ionic strength, *etc.*). Moreover, the on-demand and iterative μ-bubble generation features allow the system to be reusable even when the channel is completely filled. The proposed sweat rate monitoring device is delivered by a fully integrated hybrid microfluidic/electronic system, which was validated for on-body application through iontophoresis- and exercise-induced sweat secretion experiments on human subjects. The obtained sweat rate profiles successfully capture the subjects' physiological responses to sweat stimulus and different levels of exercise. The proposed autonomous wearable sweat rate monitoring device would provide valuable information for inferring the body's hydration/electrolyte homeostasis status in the future. The digitized microbubble detection mechanism would also play a critical role in calibrating sweat biomarkers readings, in response to variations in sweat secretion, when integrated with other sweat biosensor technologies.

4. Materials and methods

4.1 System fabrication and integration

A printed circuit board embedded with actuation and sensing gold electrodes pairs and contains the sensing and communication circuit was designed as the middle layer of the device. The microfluidic channel layer on top and the sweat collector layer (also served as skin-interfacing adhesion layer) on bottom were implemented with a cost-effective double-sided tape (3M, 300LSE, MN, USA) and polyethylene terephthalate (PET). The microchannel/structures (0.35 mm in width and 0.17 mm in height from cross view) were designed using CAD software and laser cut using a VLS 2.30. Because the microchannel/structures were made of double-sided tape materials, it will naturally adhere the PCB layer and the cover layer. The surfactant reservoir was designed with a liquid volume of 7 μL and

the surfactant deposition were performed using 5 % Pico-Surf (Sphere Fluidics, Cambridge, UK) in Novec 7500 after the device integration.

4.2 Implementation of off-body sensing characterization and calibration

For *ex situ* sensing characterization and calibration, we used the proposed microfluidic/electronic system and connected it to an external electrochemical workstation (CHI 600E) to precisely track the impedance change. A phosphate-buffered saline (PBS) solution with pH 7 was prepared in a 10 mL syringe and attached to a programmable syringe pump (Harvard Apparatus Standard Infuse/Withdraw PHD ULTRA™). During the experimental session, the pump was programmed to increase the flow rate continuously (from 0.6 μL/min to 10 μL/min). The impedance change profile was obtained and followed up with flow rate information calculation.

4.3 Implementation of interferent test

To prove the robustness of our sensing accuracy against potential external factors present in human sweat, we conducted pH, ionic strength, and temperature interference tests. All tests were designed and performed following general off-body tests as discussed above. The flow rate was programmed as a constant value of 2 μL/min for all tests. For pH and ionic strength tests, we prepared different solutions of PBS under controlled conditions where the pH was varied among 6, 7, and 8 (titrated with NaOH and HCl solution and measured using Themo Fisher Scientific AE150 pH meter), and Na^+ concentrations varied among 1 mM, 3.33 mM, and 0.1 mM. For temperature test, we created different temperature environment among 30°C, 37°C and 44°C using the hot plate. Flow rate measurements using our proposed device were performed either using solutions with different pH, ionic strength, or under different temperatures.

4.4 Circuit design

Wireless sweat rate sensing was realized with a custom-developed PCB. An onboard MCU (MSP430G2553, Texas Instrument, USA) was programmed for μ-bubble generation at on-demand time point and signal acquisition in real-time. Specifically, to generate the μ-bubble, a programmable switch (MAX14759, Maxim Integrated, USA) was utilized to connect (controlled by the MCU) the bubble generation electrodes with a programmable voltage regulator (LT3525–5, Linear Technology, USA). The impedance between the sensing electrode pairs was measured as a digital voltage output with the aid of programmable waveform generator (AD9833, Analog Devices, USA), an inverted amplifier (OPA333, Texas Instrument, USA) and a 10-bit internal ADC channel in MCU. The output profile of the waveform generator was set as a 1 kHz sinuous wave with 1 V peak-to-peak voltage. By interfacing the MCU with a Bluetooth module (HM-11, Seeed Technology Co., Ltd, China), wireless, bilateral, and real-time communication of user commands and sensing data with the user interface in a smartphone-based application was achieved.

4.5 On-body sweat rate monitoring - exercising

In order to analyze the practical and exercise-induced sweat rate information using the devised sensor, the device was tested on subjects undergoing different exercise regimens.

Subjects were mandated to exercise on a stationary bike with the device applied to their backs prior to the experiment, as depicted in fig. 4f. Once the demonstration commenced, up to 10 minutes of high-RPM (Revolutions per minute) activity was performed as pre-collection stage. Then subjects started following two different exercising intensity regimens as shown in fig. 4g, h. At around each minute, 1 μ-bubble was generated and sweat rate information was obtained and transmitted to smartphone.

4.6 On-body sweat rate monitoring - iontophoresis

In order to analyze the practical and self-induced sweat rate information using the devised sensor, the device was tested on a subject experiencing iontophoresis sweat stimulation. As demonstrated in fig. 4c. (left inset), the iontophoresis process induces sweat through the use of a voltage gradient across the epidermis, where Pilogel® Iontophoretic Discs were placed beneath electrodes. After the electrodes were placed across a segment of the arm, the Webster Sweat Inducer was activated for 5 minutes. The wearable microfluidic system was then applied to the treated skin region. The experiment spans 30 minutes during which μ-bubbles were generated and sweat rate information was obtained and transmitted to smartphone.

Supplementary Material

Refer to Web version on PubMed Central for supplementary material.

Acknowledgements

We thank the UCLA Nanoelectronics Research Facility (NRF) for providing access to device fabrication equipment. This work was supported by S.E.'s startup package provided by the UCLA Henry Samueli School of Engineering and Applied Sciences, and National Institutes of Health (Grant: R21DK128711-01),

References

1. Sempionatto JR, Lin M, Yin L, De la Paz E, Pei K, Sonsa-Ard T, de Loyola Silva AN, Khorshed AA, Zhang F, Tostado N, Xu S. and Wang J, Nat Biomed Eng, 2021, 5, 737–748. [PubMed: 33589782]
2. Yang Y, Song Y, Bo X, Min J, Pak OS, Zhu L, Wang M, Tu J, Kogan A, Zhang H, Hsiai TK, Li Z. and Gao W, Nat Biotechnol, 2020, 38, 217–224. [PubMed: 31768044]
3. Gao W, Emaminejad S, Nyein HYY, Challa S, Chen K, Peck A, Fahad HM, Ota H, Shiraki H, Kiriya D, Lien DH, Brooks GA, Davis RW and Javey A, Nature, 2016, 529, 509–514. [PubMed: 26819044]
4. Ghaffari R, Rogers JA and Ray TR, Sens Actuators B Chem, 2021, 332.
5. Emaminejad S, Gao W, Wu E, Davies ZA, Yin Yin Nyein H, Challa S, Ryan SP, Fahad HM, Chen K, Shahpar Z, Talebi S, Milla C, Javey A. and Davis RW, Proc Natl Acad Sci U S A, 2017, 114, 4625–4630. [PubMed: 28416667]
6. Cheng X, Wang B, Zhao Y, Hojaiji H, Lin S, Shih R, Lin H, Tamayosa S, Ham B, Stout P, Salahi K, Wang Z, Zhao C, Tan J. and Emaminejad S, Advanced Functional Materials, 2019, 30.
7. Kwon K, Kim JU, Deng Y, Krishnan SR, Choi J, Jang H, Lee K, Su C-J, Yoo I, Wu Y, Lipschultz L, Kim J-H, Chung TS, Wu D, Park Y, Kim T.-i., Ghaffari R, Lee S, Huang Y. and Rogers JA, Nature Electronics, 2021, 4, 302–312.
8. Huang X, Liu Y, Zhou J, Nejad SK, Wong TH, Huang Y, Li H, Yiu CK, Park W, Li J, Su J, Zhao L, Yao K, Wu M, Gao Z, Li D, Li J, Shi R. and Yu X, npj Flexible Electronics, 2022, 6.

9. Kim J, Wu Y, Luan H, Yang DS, Cho D, Kwak SS, Liu S, Ryu H, Ghaffari R. and Rogers JA, Adv Sci (Weinh), 2022, 9, e2103331.
10. Xiao J, Liu Y, Su L, Zhao D, Zhao L. and Zhang X, Anal Chem, 2019, 91, 14803–14807. [PubMed: 31553565]
11. Seki Y, Nakashima D, Shiraishi Y, Ryuzaki T, Ikura H, Miura K, Suzuki M, Watanabe T, Nagura T, Matsumato M, Nakamura M, Sato K, Fukuda K. and Katsumata Y, Sci Rep, 2021, 11, 4929. [PubMed: 33654133]
12. Raymundo-Pereira PA, Gomes NO, Machado SAS and Oliveira ON, Chemical Engineering Journal, 2022, 435.
13. Tai LC, Liaw TS, Lin Y, Nyein HYY, Bariya M, Ji W, Hettick M, Zhao C, Zhao J, Hou L, Yuan Z, Fan Z. and Javey A, Nano Lett, 2019, 19, 6346–6351. [PubMed: 31381353]
14. Lin S, Yu W, Wang B, Zhao Y, En K, Zhu J, Cheng X, Zhou C, Lin H, Wang Z, Hojaiji H, Yeung C, Milla C, Davis RW and Emaminejad S, Proc Natl Acad Sci U S A, 2020, 117, 19017–19025. [PubMed: 32719130]
15. Lin S, Wang B, Yu W, Castillo K, Hoffman C, Cheng X, Zhao Y, Gao Y, Wang Z, Lin H, Hojaiji H, Tan J. and Emaminejad S, ACS Sens, 2020, 5, 265–273. [PubMed: 31909594]
16. Yang Y. and Gao W, Chem Soc Rev, 2019, 48, 1465–1491. [PubMed: 29611861]
17. Heikenfeld J, Jajack A, Feldman B, Granger SW, Gaitonde S, Begtrup G. and Katchman BA, Nat Biotechnol, 2019, 37, 407–419. [PubMed: 30804536]
18. Bariya M, Nyein HYY and Javey A, Nature Electronics, 2018, 1, 160–171.
19. Lin H, Tan J, Zhu J, Lin S, Zhao Y, Yu W, Hojaiji H, Wang B, Yang S, Cheng X, Wang Z, Tang E, Yeung C. and Emaminejad S, Nat Commun, 2020, 11, 4405. [PubMed: 32879320]
20. Falk B. and Dotan R, Appl Physiol Nutr Metab, 2008, 33, 420–427. [PubMed: 18347699]
21. Periard JD, Eijsvogels T, Daanen HAM and Racinais S, Br J Sports Med, 2021, 55, 410–411. [PubMed: 32883691]
22. Smith JW, Bello ML and Price FG, Nutrients, 2021, 13.
23. Sim JK, Yoon S. and Cho YH, Sci Rep, 2018, 8, 1181.
24. Nyein HYY, Tai LC, Ngo QP, Chao M, Zhang GB, Gao W, Bariya M, Bullock J, Kim H, Fahad HM and Javey A, ACS Sens, 2018, 3, 944–952. [PubMed: 29741360]
25. Yuan Z, Hou L, Bariya M, Nyein HYY, Tai LC, Ji W, Li L. and Javey A, Lab Chip, 2019, 19, 3179–3189. [PubMed: 31433434]
26. Kim SB, Lee K, Raj MS, Lee B, Reeder JT, Koo J, Hourlier-Fargette A, Bandodkar AJ, Won SM, Sekine Y, Choi J, Zhang Y, Yoon J, Kim BH, Yun Y, Lee S, Shin J, Kim J, Ghaffari R. and Rogers JA, Small, 2018, 14, e1802876.
27. Matzeu G, Fay C, Vaillant A, Coyle S. and Diamond D, IEEE Trans Biomed Eng, 2016, 63, 1672–1680. [PubMed: 26394409]
28. Francis J, Stamper I, Heikenfeld J. and Gomez EF, Lab Chip, 2018, 19, 178–185. [PubMed: 30525141]
29. Lin H, Zhao Y, Lin S, Wang B, Yeung C, Cheng X, Wang Z, Cai T, Yu W, King K, Tan J, Salahi K, Hojaiji H. and Emaminejad S, Lab Chip, 2019, 19, 2844–2853. [PubMed: 31359008]
30. Abdelwahed MAB, Wielhorski Y, Bizet L. and Bréard J, Journal of Composite Materials, 2012, 48, 37–48.

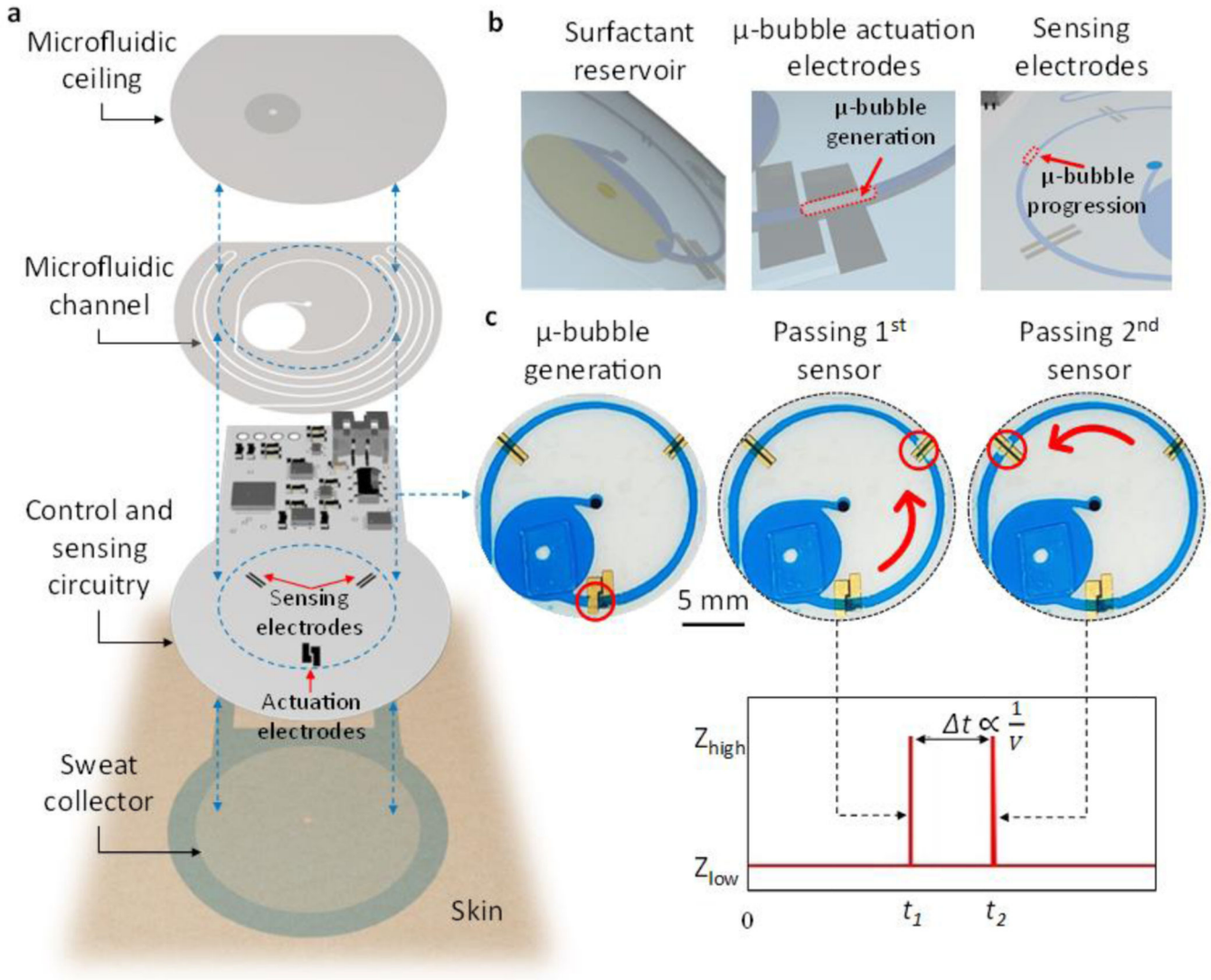

Fig. 1: A wearable hybrid microfluidic/electronic system for autonomous sweat rate monitoring.

a Exploded view of the hybrid microfluidic/electronic system, which is constructed through the vertical integration of a tape-based sweat collector film, a PCB-based layer (featuring the electrolysis and impedance sensing electrodes and the associated circuitries), and a microfluidic module (containing a surfactant reservoir and a spiral serpentine channel to facilitate μ-bubble progression). **b** Localized view of the functional microfluidic components: surfactant reservoir, electrolysis electrode pair for μ-bubble generation, and sensing electrodes. **c** Our devised flow rate measurement methodology for sweat rate monitoring, which is based on tracking the generated μ-bubble's passage time across two impedance sensing electrode pairs.

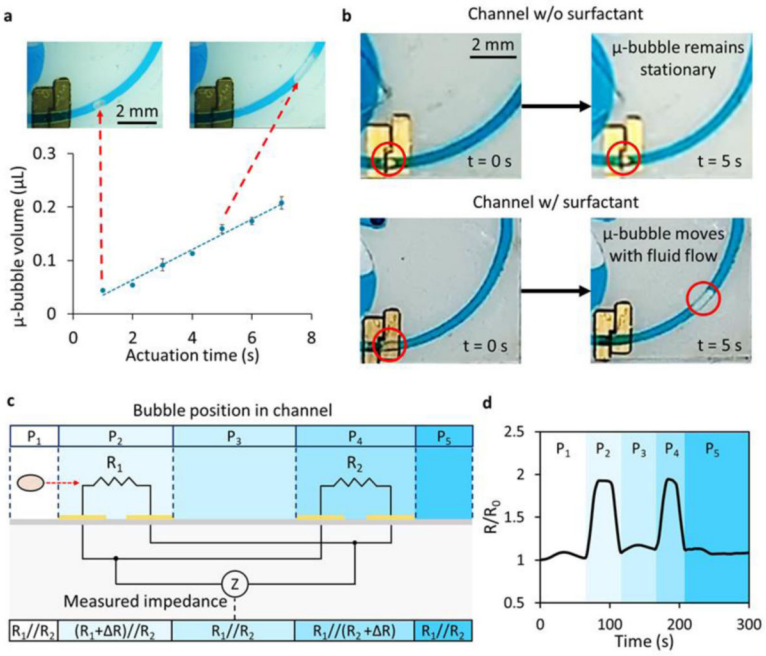

Fig. 2: Characterization and demonstration of functional microfluidic components for digitized μ-bubble detection.

a μ-bubble generation characterization: electrolysis duration *vs.* μ-bubble size ($n = 3$, error bars indicate standard error). **b** Optical images of surfactant-treated/untreated μ-bubble progression within the microfluidic channel. **c** First-order equivalent circuit model of the sensing mechanism. Corresponding μ-bubble positions in the channel are labeled through P_1 to P_5 with representative color. R_1 and R_2 refer to the resistance of the channel as respectively measured by the first and second neighboring electrode pairs. ΔR is the change in channel resistance caused by the passage of the generated μ-bubble above each of the neighboring electrode pairs. **d** A representative experimentally measured relative impedance as the generated μ-bubble moving from the phase P_1 to P_5.

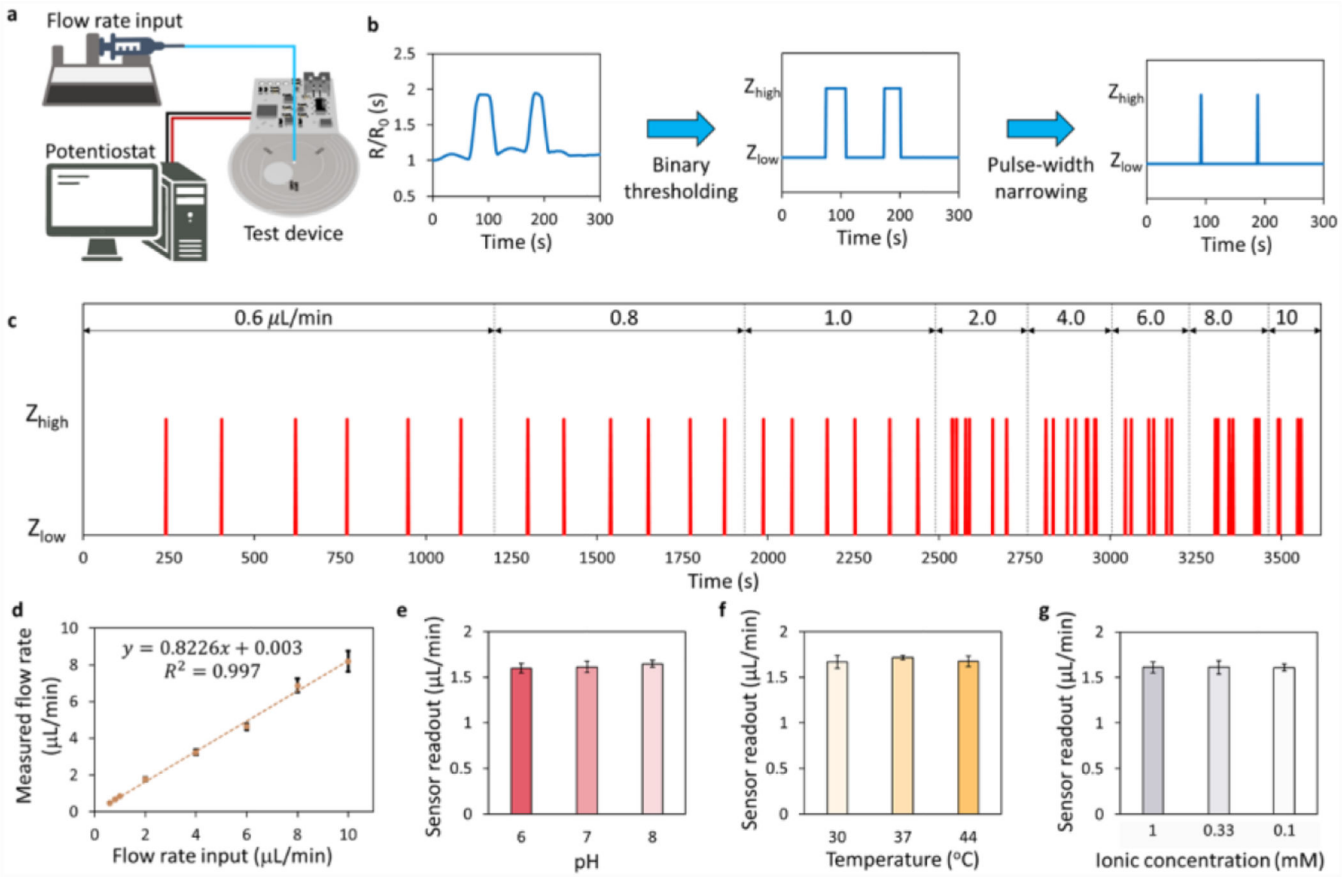

Fig. 3: *Ex situ* test of the sweat rate sensing system.

a Experiment setup for *ex situ* sweat rate sensing. **b** Signal processing procedure. **c** Real-time impedance readouts with progressively increasing flow rate input (impedance measured at 1 kHz). **d** Calibration curve of the measured flow rates vs. input flow rates. The flow rate is estimated via $v = V/\Delta t$, where V is the volume of the channel between two impedance sensing electrode pairs, and Δt is the time interval between two adjacent impedance spikes (Z_{high}), considered as the μ-bubble's flow time. The linear relationship allows for the correction of the systematic error. **e-g** Sweat rate sensor interference test at various (**e**) pH, (**f**) temperature, and (**g**) ionic strength (1 mM, 0.33 mM, and 0.1 mM Na^+ in phosphate buffered saline, PBS).

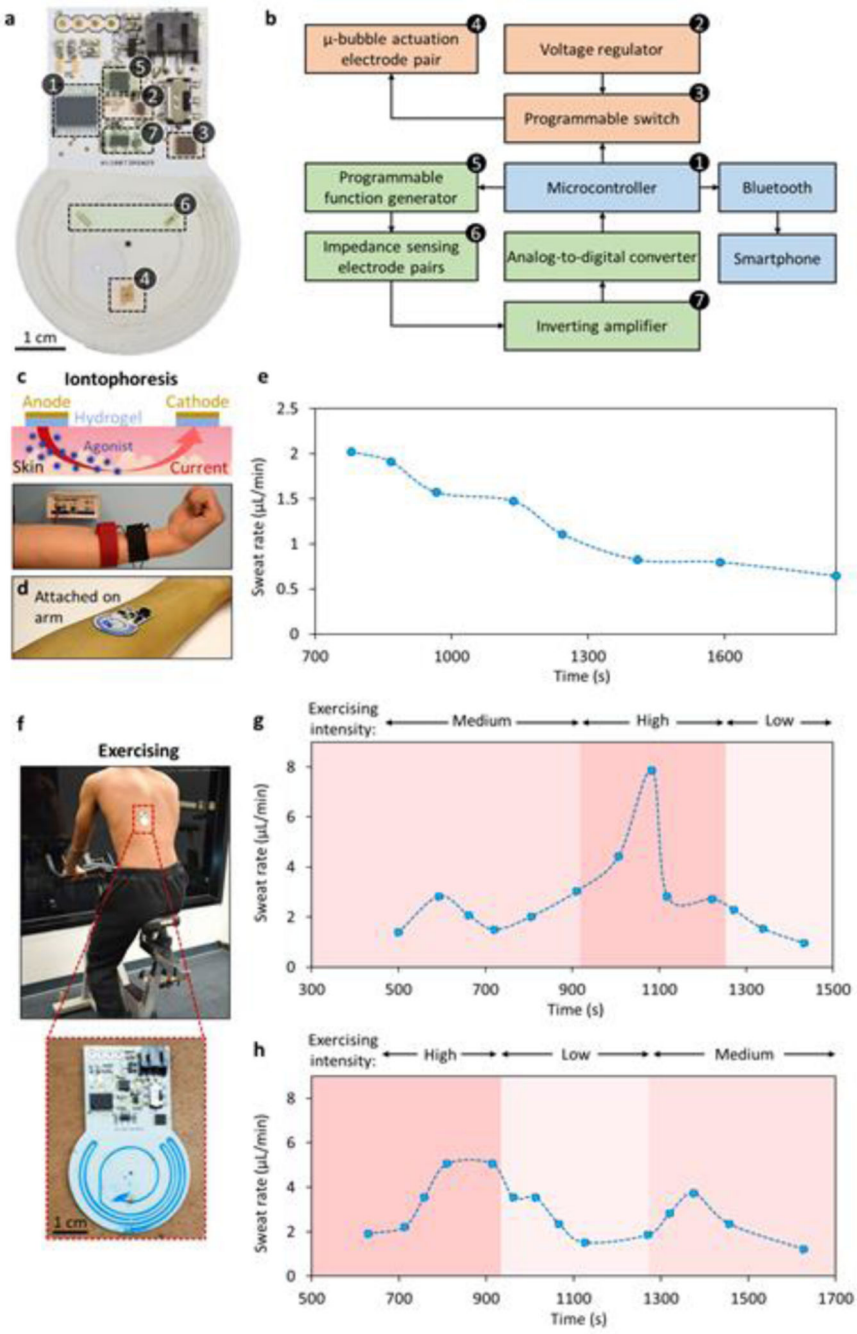

Fig. 4: On-body application of the fully-integrated wearable sweat rate sensing system.

a Optical image and **b** system-level diagram of the custom-developed PCB, equipped with wireless actuation and sensing capabilities, which monolithically integrates μ-bubble generation and tracking electrodes. **c** Photograph of sweat stimulation in a sedentary subject with schematic of the iontophoresis operation. **d** Photograph of fully-integrated wearable sweat rate sensing system applied on the iontophoresis stimulated arm. **e** Iontophoretically-induced sweat rate profile on a subject. **f** Photograph of a subject engaged in exercising (stationary cycling) with the fully integrated wearable sweat rate sensing system placed on

the back. **g,h** In-situ exercise-induced sweat rate monitoring results for two subjects under two different exercising intensity schedules.